Characterization of Al_2Ti/Al_3Ti-based intermetallic and Al_2O_3/TiO_2-based oxide composite coatings fabricated on Ti6Al4V alloy

Salim Levent Aktuğ[1]*, Doğan Acar[2], Ömer Necati Cora[2], Salih Durdu[3,4]

[1] *Department of Materials Science and Engineering, Gebze Technical University, Gebze, Kocaeli 41400, Turkey*
[2] *Department of Mechanical Engineering, Karadeniz Technical University, Trabzon 61000, Turkey*
[3] *Department of Industrial Engineering, Giresun University, Giresun 28200, Turkey*
[4] *Department of Mechanical Engineering, Giresun University, Giresun 28200, Turkey*

Abstract

In this work, an aerospace-grade Ti6Al4V alloy was coated by electro spark deposition (ESD), micro-arc oxidation (MAO), and combined ESD + MAO coating methods to improve mechanical properties and wear resistance. The results obtained from the coatings were compared with the bare Ti6Al4V. The phase structure, surface-cross sectional morphologies, elemental distribution, surface-cross sectional mechanical and wear properties of the bare alloy and the coatings were investigated by XRD, SEM, EDX-mapping, nanoindentation, micro--Vickers hardness, and tribometer. The XRD results revealed that the MAO and ESD + MAO duplex coatings contained rutile-TiO_2 and γ-Al_2O_3 phases, while Al_3Ti, Al_2Ti, and $AlTi_3$ phases were observed in the ESD coating. The average hardness of all coatings was significantly improved with respect to bare Ti6Al4V due to the crystalline and dense structure of the inner layer. In addition, the wear resistance of the coatings was significantly improved compared to that of bare Ti6Al4V.

K e y   w o r d s: micro-arc oxidation (MAO), electro spark deposition (ESD), Al_2O_3/TiO_2 composite, mechanical properties, tribological properties

1. Introduction

The titanium alloy (Ti6Al4V) is used in chemical industries, medical implants, and aerospace applications due to its special properties, such as high strength-to-weight ratio, corrosion resistance, and biocompatibility [1, 2]. However, Ti6Al4V alloy has low hardness and poor wear resistance [3, 4]. Thus, its surface properties are improved by various coating processes such as physical vapor deposition (PVD) [5], chemical vapor deposition (CVD) [6], and plasma spray [7, 8]. However, the preparation processes of these methods are complicated, the equipment cost is relatively high, and the adhesion is poor [2]. The ESD technique, which uses rapid electrical power discharges to transfer material from the conductive electrode to a conductive substrate, is a pulsed

micro-welding process under environmental conditions (atmosphere/argon). A plasma arc is generated from 8000 to 25,000 °C by the direct current between the substrate and the electrode tip when the capacitor energy is released. Eventually, the consumable electrode is ionized by the plasma arc, and a small amount of molten electrode material is transferred onto the substrate [9]. ESD technique can be applied to the complex-shaped surface and has some advantages such as excellent effect–cost ratio, small heat-affected zone, and metallurgical bond interface. The ESD can prolong the service life of the materials by using high-temperature oxidation-resistant material, hardening material, and wear-resistant material [10–12].

The MAO technique, an electrochemical surface treatment process, is widely used to form a ceramic film on nonferrous metal surfaces to improve hard-

ness, corrosion resistance, and wear resistance [13, 14]. A passive layer forms on the substrate at the first stages of the MAO process. At the next stage of the MAO process, numerous gas bubbles are generated. This stage refers to anodic oxidation resulting in a porous insulation film [15, 16]. A plasma discharge occurs when the applied voltage exceeds the breakdown voltage. Subsequently, a localized molten channel is formed at the micro-discharge zone. After electrochemical reactions, the produced molten oxides are ejected from micro-discharge channels with a volcano-like movement, and they are solidified rapidly by the electrolyte. This led to forming porous pancake-like regions. The coating repeatedly grows throughout its thickness by repeating steps of micro-discharge formation [17].

There are a few literature studies on the fabrication and characterization of duplex coatings on ferrous metals by combined ESD and MAO in the last decade [18–20]. In our previous works, the duplex coatings were fabricated on steel substrates by using combined ESD and MAO techniques [18–20]. However, there is no study on the fabrication, characterization, and investigation of mechanical (hardness) and tribological (friction and wear) properties of the ESD + MAO coating system together with ESD and MAO coating techniques on ASTM B205-90 Grade 5 Ti6Al4V alloy.

In this work, the intermetallic- and oxide-based single and duplex coatings were produced on Ti6Al4V alloy (AMS4911F&H, ASTM B205-90 Grade 5) by using ESD, MAO, and combined ESD + MAO techniques to improve the mechanical and tribological properties of Ti6Al4V. Subsequently, bare Ti6Al4V and all coatings were characterized by surface characterization techniques such as XRD, SEM, EDX, and thickness measurements. Furthermore, their surface and cross-sectional mechanical properties and tribological properties were examined in detail.

2. Experimental details

2.1. Sample preparations

The rectangular Ti6Al4V alloy sheets (manufactured per Aerospace Materials Standard (AMS4911F &H, ASTM B205-90 Grade 5)) with 10 mm × 10 mm × 0.67 mm in thickness were used as a substrate material. During pre-treatment coating processes, the surfaces of Ti6Al4V were ground with SiC sandpapers up to 1200 grit. After that, the surface of the titanium sheets was cleaned in an ultrasonic bath and kept at a desiccator.

2.2. Electro-spark deposition (ESD) process

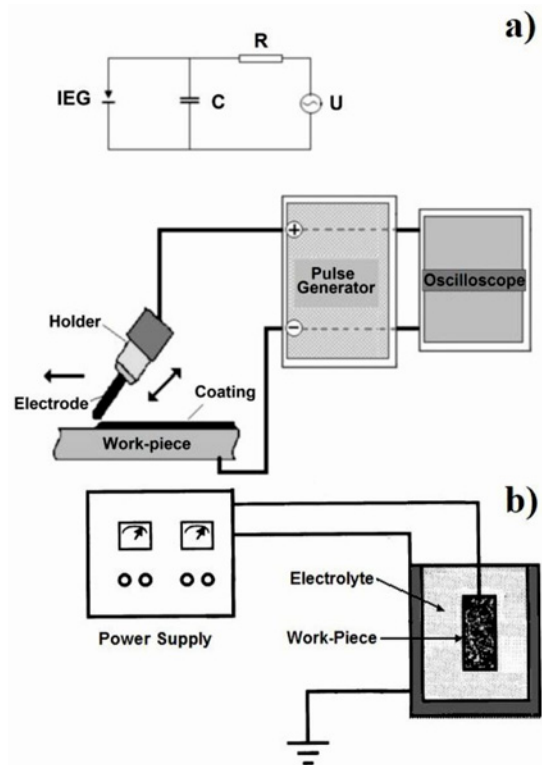In this step, pure Al was deposited on the Ti6Al4V

Fig. 1. Schematic representation of the coating systems set up: (a) ESD device and (b) MAO [18].

alloy substrate by a special ESD device. A schematic representation of the ESD device is given in Fig. 1a. In our previous studies, the ESD system was comprehensively described [18, 21]. Through the ESD, the power consumption and the stabilized voltage output were kept at 180 W and 40 V, respectively. The ESD treatment was performed using a hand-held applicator under ambient temperature in unipolar mode. The voltage between the substrate and electrode reduced at 17 V, and the electricity was stable at 3 C. The ESD was performed under argon conditions with a series of rectangular pulses of 100 μs duration and current amplitude of 100 A. The estimated pulse frequencies were approximately 100 Hz.

2.3. Micro-arc oxidation (MAO) process

In this step, the oxide-based layers on the Ti6Al4V substrate and ESD-coated Ti6Al4V substrates were fabricated by the MAO device applying bipolar impulses. A schematic representation of the MAO device is given in Fig. 1b. The electrolyte solution was prepared by mixing 20 g L^{-1} NaAlO$_2$ (#CAS: 1138-49-1 Sigma Aldrich) and 2 g L^{-1} KOH (#CAS: 1310-58-3 VWR Chemicals) in distilled water. The substrate and stainless steel container served as anode and cathode, respectively. The current density was measured as 0.25 A cm^{-2} for 10 min through the MAO process.
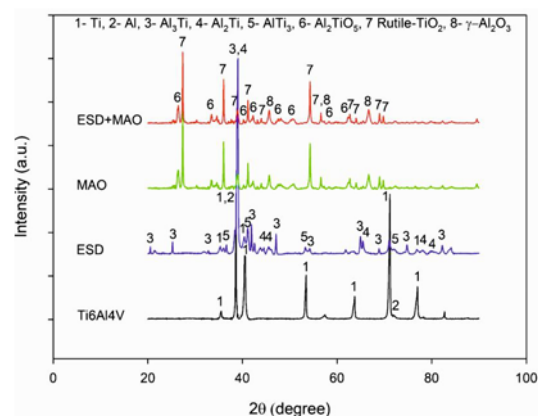
Fig. 2. XRD spectra of bare Ti6Al4V alloy, ESD-coated Ti6Al4V, MAO-coated Ti6Al4V, and ESD + MAO-coated Ti6Al4V surfaces.

2.4. Characterization of the coatings

The phase composition of bare Ti6Al4V, ESD--coated Ti6Al4V, MAO-coated Ti6Al4V, and the ESD + MAO layers was investigated by X-ray diffractometer (XRD, Bruker D8 Advance). The XRD was carried out in the range of 20° to 90°, at a scanning speed of $1° \min^{-1}$. Surface and cross-sectional morphologies of bare alloy and the coatings were examined by a scanning electron microscope (SEM, Philips XL 30 SFEG). Also, the elemental distribution of the surfaces was analyzed by an EDX-mapping attached to SEM. The hardness values of bare Ti6Al4V, ESD, MAO, and ESD + MAO surfaces were evaluated by a nanoindentation tester device (Hysitron TI 950). The five indentations were applied up to the maximum load of $500 \, \mu N$ onto all surfaces by a Berkovich indenter. The hardness measurements through the substrate cross-section and the coatings were carried out at $50 \, g$ for $5 \, s$ by a microhardness tester (Anton Paar MHT-10). The metallographic analysis was carried out using an SEM. The tribological behaviors of bare Ti6Al4V alloy, ESD, MAO, and ESD + MAO coatings were investigated through $30 \, m$ under N at room temperature and dry conditions by using an Al_2O_3 ball (diameter of $6 \, mm$) standard reciprocating ball-on-disc tribometer (CSM Instruments).

3. Results and discussion

3.1. Phase structures

The XRD phase spectra images of bare Ti6Al4V, ESD-coated Ti6Al4V, MAO-coated Ti6Al4V, and ESD + MAO-coated Ti6Al4V surfaces are given in Fig. 2. As expected, the Ti (JCPDS card number: 44-1294) and Al (JCPDS card number: 4-0787) phases

were obtained on bare Ti6Al4V alloy. However, the V phase was not detected, whereas it exists in the alloy structure. In addition, Al_3Ti (JCPDS card number: 37-1449), Al_2Ti (JCPDS card number: 52-0861), and $AlTi_3$ (JCPDS card number: 52-0859) intermetallic phases were observed on ESD-coated Ti6Al4V alloy surface. The existence of the Al_3Ti, Al_2Ti, and $AlTi_3$ phases is directly related to the Al alloying on the Ti6Al4V substrate. The ESD-coated layers did not contain the oxide-based phases as the process was carried out under argon atmosphere conditions. Moreover, oxide-based phase structures were detected on both MAO and ESD + MAO surfaces. Except for oxide-based phases, the other intermetallic phases were not detected on the ESD + MAO surface since the X-rays could not penetrate deeper than a few micrometers. Thus, Al_2TiO_5 (JCPDS card number: 26-0040), stable rutile-TiO_2 (JCPDS card number: 21-1276), and metastable γ-Al_2O_3 (JCPDS card number: 50-0741) oxide-based phases were observed as major phases on both MAO and duplex coating surfaces. As known from the literature, the Al_3Ti, Al_2Ti, and $AlTi_3$ intermetallic structures have covalent bonding [22]. Also, minor Ti and Al elemental structures exist in the ESD coating layer. These structures ionize to positively charge cationic ions such as Ti^{4+} and Al^{3+} during the MAO process. Thus, cationic and anionic compounds (O^{2-} and OH^-) react with each other in micro-discharge channels under high temperatures of up to $3000 \, K$ and high pressure through the MAO process due to the existence of oppositely charged ions [23]. Finally, oxide-based such as Al_2TiO_5, TiO_2, and γ-Al_2O_3 phases form on the MAO-coated surfaces. The intermetallic and oxide-based phases observed on all coating surfaces improve mechanical properties such as hardness and tribological properties. However, the outer layers of ESD and MAO coatings contain amorphous phases due to the rapid solidification nature under the atmosphere (for the ESD process) [24] and electrolyte conditions (for the MAO process) [25, 26]. Thus, the outer layers of these coatings are insufficient to carry loads.

3.2. Surface morphologies

The surface morphologies of bare Ti6Al4V, ESD-coated Ti6Al4V, MAO-coated Ti6Al4V, and ESD + MAO-coated Ti6Al4V surfaces are shown in Fig. 3. There are some parallel traces on the bare Ti6Al4V alloy surface during the post-grinding process. As the molten Al electrode splash hits the surface during the ESD technique, the ESD-coated surface is rough and irregular due to the local alloying process [27]. Also, thermal cracks occur on the surface due to the rapid shrinkage of the coating formed by melted electrodes that contact Ti6Al4V alloy under atmospheric conditions. Thus, as the amount of melt coming from
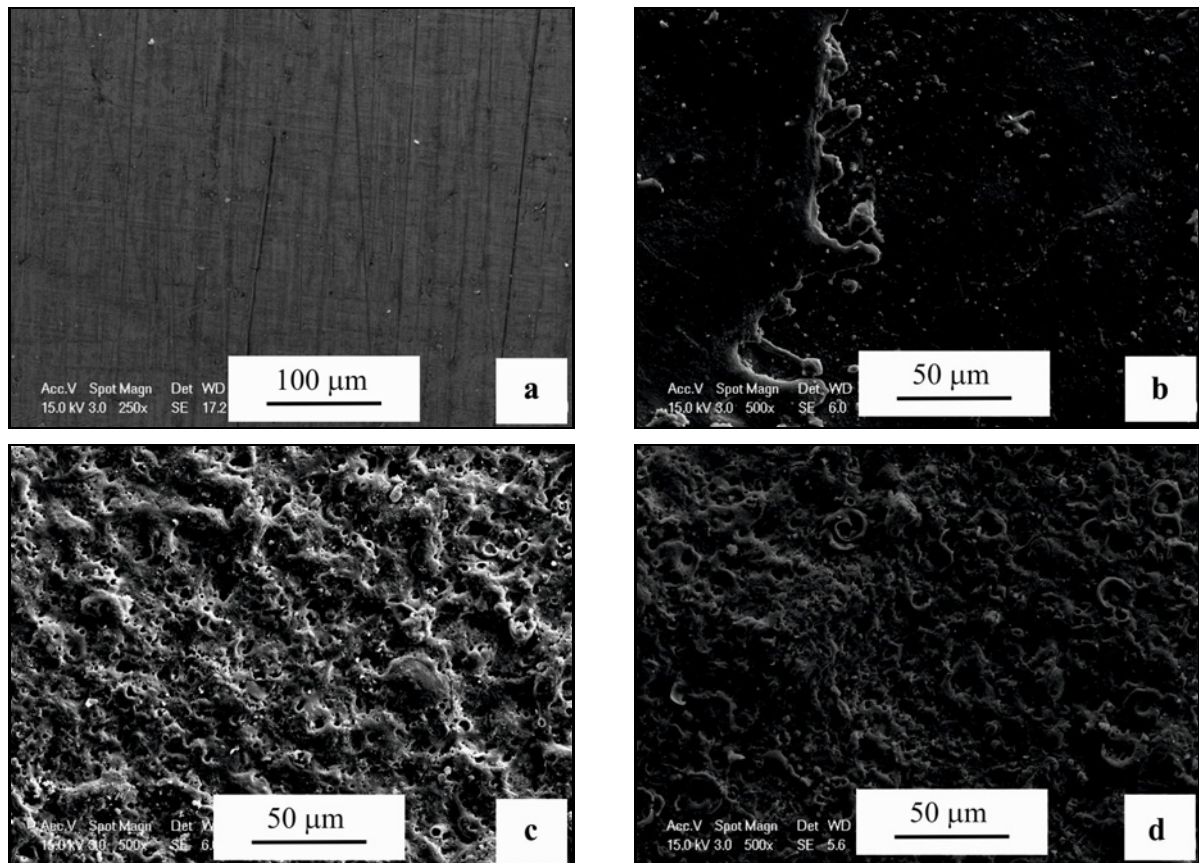
Fig. 3. The surface morphologies of the samples: (a) bare Ti6Al4V alloy, (b) ESD coating, (c) MAO coating, and (d) ESD + MAO coating.

the electrode increases on the surface, the probability of crack formation decreases. Eventually, the freezing rate and the chance of cracking are reduced [28]. Moreover, all MAO and ESD + MAO coatings yielded typical volcano crater-like porous structures, as shown in Figs. 3c and 3d. These structures consist of many micro-pores and micro-cracks. The surfaces of MAO and ESD + MAO were porous and rough due to the presence of micro-sparks (micro-discharge channels) that occurred through the MAO technique. The micro-pores occurred by molten oxide and gas bubbles overflowing from micro-discharge channels. Also, the micro-cracks near the micro-discharge channels resulted from thermal stresses due to the rapid solidification of melted coating contacted to relatively cold electrolytes during the MAO [29]. However, the thermal cracks on the ESD + MAO surface were more than those on the MAO, as seen in Figs. 3b–d. Also, the MAO surface is homogeneous with respect to the ESD + MAO surface.

3.3. Elemental distribution

The elemental profiles of ESD, MAO, and ESD + MAO coatings were examined by EDS mapping, as shown in Fig. 4. The Ti, O, Al, and V elements were observed on all coating surfaces. The Ti, Al, and V elements detected on the ESD surface originated in the Ti6Al4V substrate and Al layer. Similarly, the Ti, Al, and V elements obtained on the MAO surface come from Ti6Al4V substrate and anionic oxide compounds in the MAO electrolyte. This implies a formation of Al_3Ti, Al_2Ti, and $AlTi_3$-based structures in the ESD layer. Also, a trace of the O element was locally detected on the ESD surface as supported by XRD. It is also noted that the V phase was not detected in the XRD analysis. However, according to EDS analysis, it was determined on the coating. This may be attributed to the amorphous structure of a low amount of V-related components in the coatings. In addition, the Ti, Al, V, and O elements detected on the ESD + MAO surface originated in the Ti6Al4V substrate, ESD, and MAO layers. These findings support the existence of Al_2TiO_5, rutile-TiO_2, and γ-Al_2O_3 on the MAO and ESD + MAO surface. The existence of Al and O in the outer layer of ESD + MAO contributes to the formation of γ-Al_2O_3. Furthermore, all elements were homogeneously distributed through the surface. However, the dark regions monitored on ESD, MAO, and ESD + MAO surfaces correspond to the micro-pore structure on the coatings. All elements
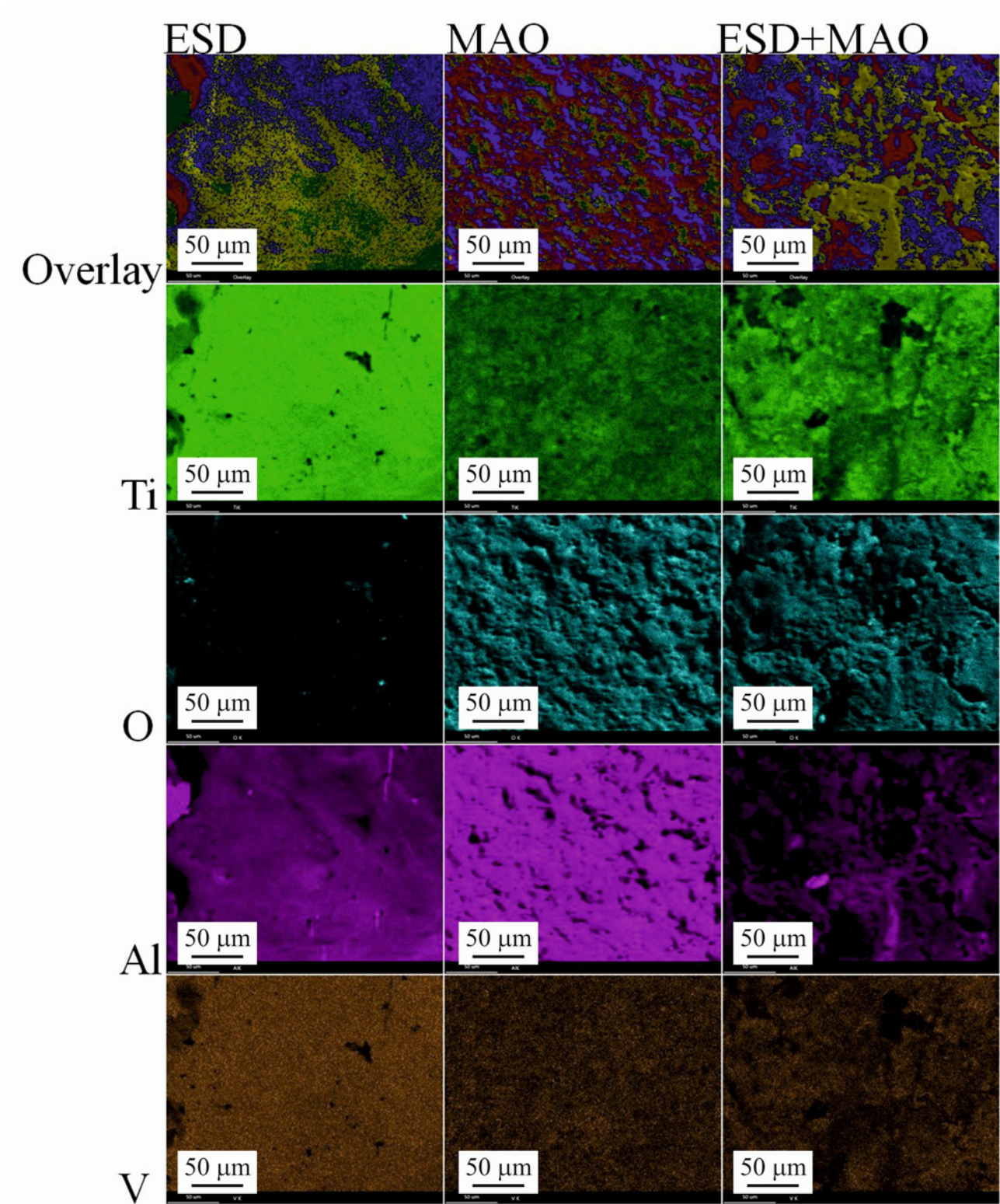
Fig. 4. The surface EDX-mapping images of ESD, MAO, and ESD + MAO coatings: (a) Overlay, (b) Ti, (c) O, (d) Al, and (e) V.

are uniformly distributed through the coatings. However, the overlay mapping images indicate that the phase structure of the MAO surface is homogeneously obtained compared to ESD and ESD + MAO surfaces.
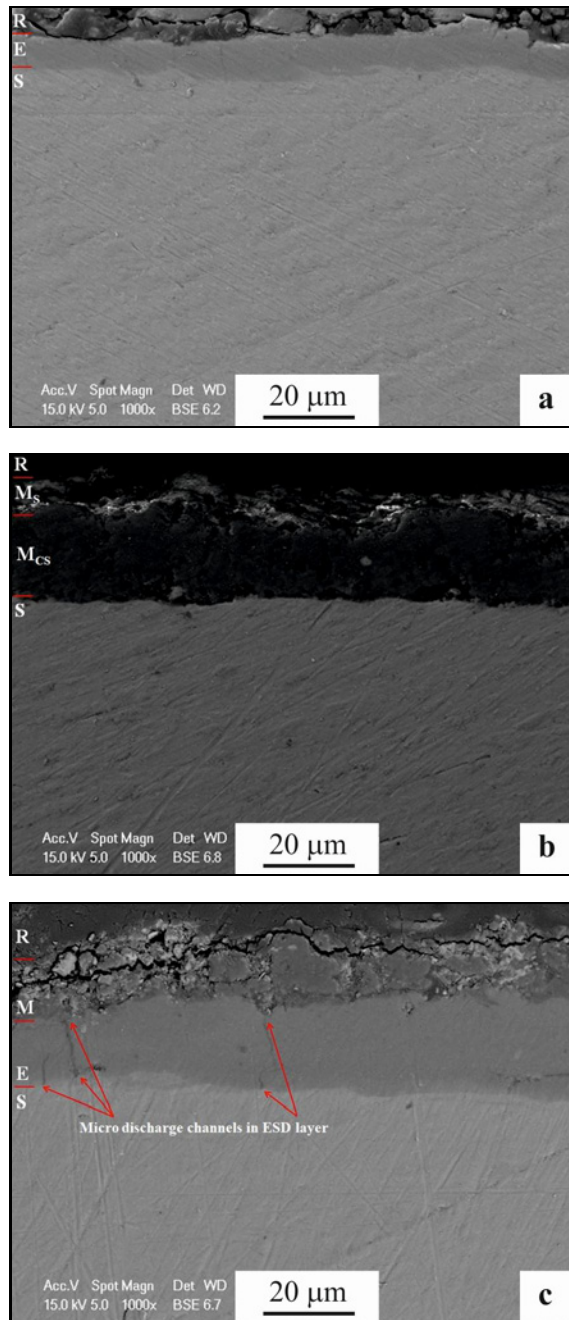
Fig. 5. The cross-sectional morphology of the samples: (a) ESD coating, (b) MAO coating, and (c) ESD + MAO coating (S: Ti6Al4V, E: ESD, M: MAO, M$_S$: MAO surface, M$_{CS}$: MAO coating region, and R: epofix resin).

3.4. Cross-sectional microstructure and thickness

The cross-sectional microstructures of ESD, MAO, and ESD + MAO coatings are displayed in Fig. 5. The average coating thicknesses of ESD, MAO, and ESD + MAO layers were approximately measured as 10.7 ± 3.3 μm, 18.4 ± 2.3 μm, and 38.63 ± 5.2 μm, re-

T a b l e 1. Nanoindentation test results such as hardness (H, MPa) of bare Ti6Al4V, ESD, MAO, and ESD + MAO surfaces

	Samples			
	Bare Ti6Al4V	ESD	MAO	ESD + MAO
Hardness (MPa)	4610	2070	870	440

spectively. According to these pictures, the ESD coating layer was locally depleted, and then, the MAO process was carried out on the Ti6Al4V substrate. The molten Al electrode hit on Ti6Al4V surface through the ESD process resulting in a dense ESD layer on Ti6Al4V alloy, as shown in Fig. 5a. However, the micro-pores originating from micro-sparks through the MAO process were observed in the cross-sectional MAO layer. Micro-discharge channels exist starting from the substrate to the outer MAO layer due to the MAO process's nature [30, 31]. The coating fabricated by combined ESD and MAO contains two layers (the duplex structure), as shown in Fig. 5c. Similar ESD and MAO microstructures were monitored on the ESD + MAO duplex layer. In addition, the presence of micro-discharge channels was clearly observed from the Ti6Al4V substrate to the outer layer of ESD coating, as seen in Fig. 5c. The melted Ti structure moves through the ESD layer and reacts with other anionic compounds in the electrolyte by the MAO process. This supports the existence of rutile-TiO_2 detected on the ESD + MAO surface and γ-Al_2O_3. Also, the MAO layer in Figs. 5b,c indicates the spongy morphological feature of the deposition along with the presence of pores.

3.5. Vickers and nanoindentation hardness measurements

The average hardness values measured on the surfaces of Ti6Al4V, ESD, MAO, and ESD + MAO are given in Table 1. Average hardness values of bare Ti6Al4V, ESD, MAO, and ESD + MAO surfaces were measured as 4610, 2070, 870, and 440 MPa, respectively. Furthermore, the outer layer of Ti6Al4V alloy consists of a naturally formed passive TiO_2 layer. This passive and dense layer protects Ti6Al4V alloy against corrosion. Initially, nanoindenter contacts with this passive oxide layer and could penetrate into the metallic layer due to very low loads of nanoindenter. The average hardness of Ti6Al4V alloys was approximately 3250 and 3600 MPa [32, 33]. However, the hardness of bare Ti6Al4V alloy is a little bit high compared to literature values. The possible reason for this could be that the hardness measurement on both metallic and passive oxide regions was carried out for
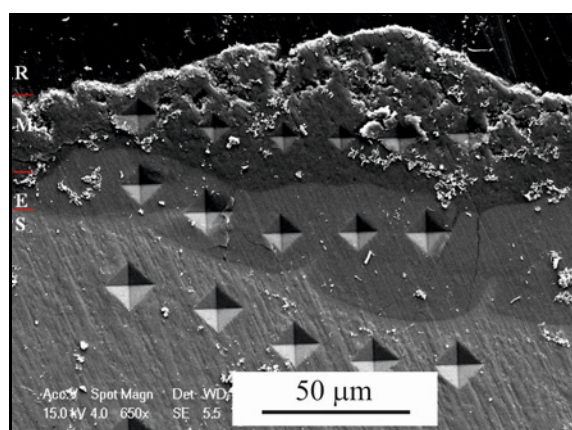
Fig. 6. Micro-Vickers indents images through cross sectional area of the bare Ti6Al4V alloy ESD + MAO coating (S: Ti6Al4V, E: ESD, M: MAO, and R: epofix resin).

Ti6Al4V alloys. It is expected that the oxide- and intermetallic-based coatings generally have superior mechanical properties, such as hardness values, compared to uncoated metal substrates due to the presence of oxide and intermetallic structures with high hardness. The current study observed the maximum surface hardness on Ti6Al4V alloy. The hardness depends on many parameters, such as the phase structure, crystalline/amorphous phases, and dense/porous structure [34, 35]. The ESD, MAO, and ESD + MAO contain oxide- and intermetallic-based phases with high hardness with respect to bare Ti6Al4V. However, the outer layer of the MAO and ESD + MAO coatings is porous (loose) and amorphous owing to micro-sparks and rapid solidification through the process. Similarly, the outer layer of the ESD coatings is amorphous since the melted structure is rapidly solidified. Thus, the outer hardness values of the surface of ESD, MAO, and ESD + MAO were lower than that for bare Ti6Al4V alloy, as expected. This is strongly related to the amorphous/crystalline phase and morphological structure (dense/loose) of the surface. Since the time required for the phase transformation from the amorphous structure to the crystalline structure was insufficient, the structures obtained during the MAO process were amorphous due to the rapid solidification of melted compounds [36–38]. As a result, the outer layer of these coatings is easily worn owing to the existence of amorphous phases. Another reason for the low mechanical values was that the outer layer of these coatings was much looser and porous compared to the inner layer [39]. Especially for the MAO coatings, there are two regions: the inner layer and the outer layer on the coatings. Micro-arc discharge can generate high temperatures of up to 3000 K in micro-discharge channels [40]. Eventually, the inner layer was a dense structure due to the sintering effect of the MAO process.

The SEM images of micro-Vickers hardness traces of bare Ti6Al4V alloy, ESD, MAO, and ESD + MAO coatings through the cross-sectional area were displayed in Fig. 6. The average hardness values of bare Ti6Al4V, ESD, and MAO coatings were approximately 337.4, 439.4, and 809.1 MPa, respectively. The results are in accordance with the studies of Kováčik et al. [41]. As shown in Fig. 6, the minimum hardness traces were observed on bare Ti6Al4V alloy. Unlike the outer layer of the coatings, the inner layers consist of dense crystalline phases. Thus, the hardness traces of these regions are small compared to bare Ti6Al4V alloy, as seen in Fig. 6. The average microhardness values of the ESD, MAO, and ESD + MAO are evaluated superior to bare Ti6Al4V because the coatings mainly contained oxide- and intermetallic-based phases with high hardness, as given in Fig. 2. The small hardness traces were clearly observed at the MAO coating while the large hardness traces were noted at bare Ti6Al4V alloy on ESD + MAO coatings, as seen in Fig. 6c. The expanding hardness traces were monitored in MAO, ESD, and uncoated Ti6Al4V alloy, respectively. This strongly depends on the dense and crystalline phase structure of the inner layers of the coatings with respect to bare alloy. As a result of these, the average hardness of the ESD, MAO, and ESD + MAO is higher than that of bare Ti6Al4V alloy.

3.6. Tribological tests

The friction coefficient variations versus the distance of bare Ti6Al4V, ESD, MAO, and ESD + MAO-coated surfaces are shown in Fig. 7. To create a new worn trace on bare Ti6Al4V surface, the friction coefficient quickly increases at the initial stages of the test as seen in Fig. 7a. After a wear trace formed on the Ti6Al4V surface, the friction coefficient decreases slowly at about sliding distance up to 10 m and remains constant afterward. However, the friction coefficients of the ESD, MAO, and ESD + MAO coatings indicated a nonlinear curve behavior. After wear trace formation, zigzag-shaped curves were observed on the surfaces of ESD and MAO coatings. It can be stated that this may be related to rough and porous surface structures. Nevertheless, in general, the friction coefficients of the ESD and MAO surfaces show a relatively stable trend throughout the test. Unlike ESD and MAO coatings, the friction coefficient of ESD + MAO alloy slowly increases at the first stages of the wear test, as seen in Fig. 7d. Then, it decreases slowly up to the sliding distance of 20 m and remains constant during the rest of the wear test. Except for the MAO, the friction coefficients of coatings were quickly increased at the initial stages of the test and reached a stable condition in the last stages of the test. At the initial stages, the outer layer of ESD, MAO, and ESD + MAO consisting of porous, loose, and amorphous structures was easily removed, as seen in Figs. 7b–d.
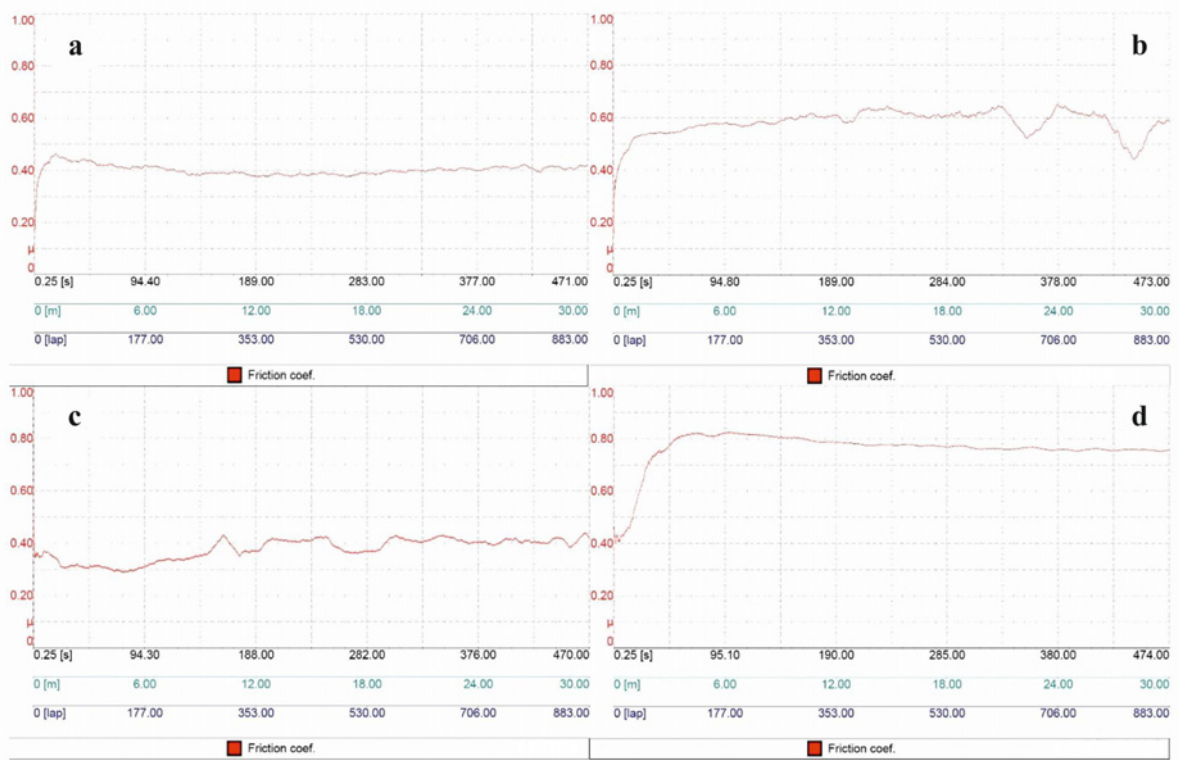
Fig. 7. The friction coefficient variations against the sliding distance: (a) bare Ti6Al4V alloy, (b) ESD, (c) MAO, and (d) ESD + MAO.
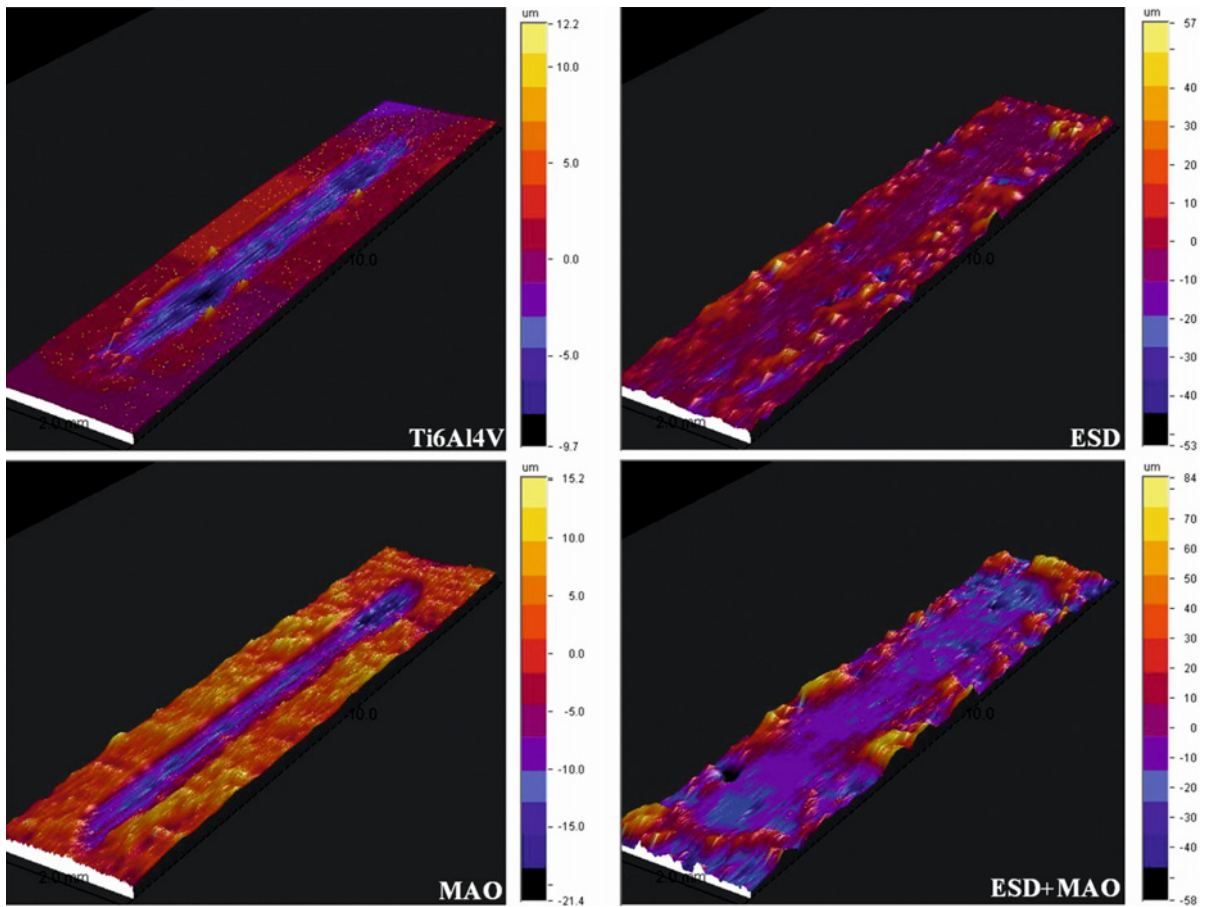

Fig. 8. Surface profilometer mapping scans through wear track regions of bare Ti6Al4V alloy, ESD, MAO and ESD + MAO coatings.
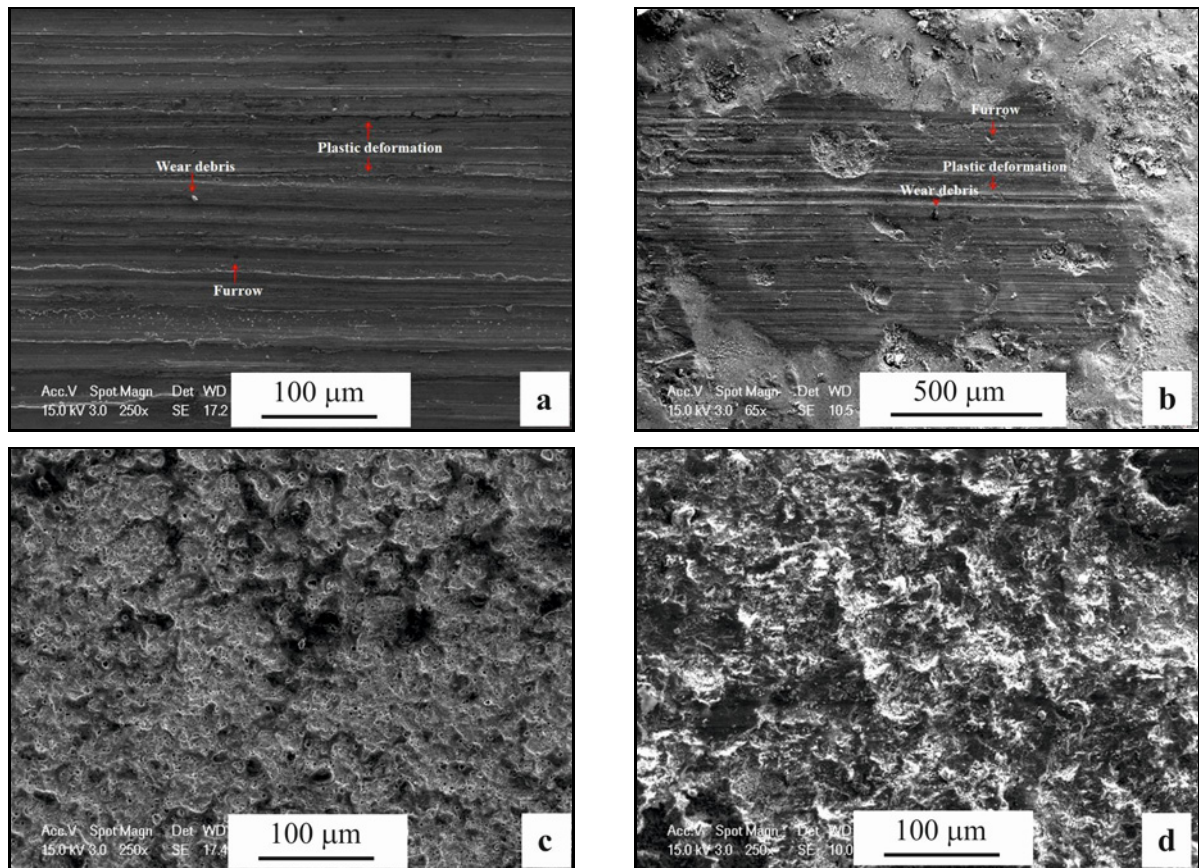
Fig. 9. Wear track SEM images of the samples: (a) bare Ti6Al4V, (b) ESD, (c) MAO, and (d) ESD + MAO.

At the following stages of the test, the friction coefficients of the coatings tend to decrease to a level and then become stable as the inner layer of the coatings is crystalline and dense compared to the outer layer. The 3D mapping profile images through the wear tracks are provided in Fig. 8. From these images, the outer layers of ESD, MAO, and ESD + MAO surfaces that were porous and rough were removed, and the surface was flattened to the dense layer. The dense layer has preserved its existence. As shown in Fig. 8, the minimum wear rates were obtained for the MAO coating, and the maximum wear rates were obtained at bare Ti6Al4V alloy. The order of the coatings in terms of wear resistance from the highest to the lowest is MAO, ESD, ESD + MAO, and uncoated Ti6Al4V alloy, respectively.

The worn surface appearances of the bare substrate and the coatings are given in Fig. 9. For bare Ti6Al4V alloy, plastic deformation, wear debris, and furrow are observed. The worn surface contains grooves aligned in the sliding direction. Thus, the dominant wear mechanism of this type of morphology refers to adhesive wear and micro-cutting, as shown in Fig. 9a. The surface is normally and tangentially exposed to the load through the contact points in the wear test. Eventually, normal and shear stresses form the micro-reliefs on the

substrate. Thus, the micro-embossment may produce plastic deformation under shear stress effects due to wear debris formation with reciprocating of the load. Moreover, the normal stress conveyed through the normal direction caused to occur some scratches and furrows on the substrate. The metal on both sides of the furrow underwent deformation and deposition. The debris accumulated during the progressive wear process flattens out again and eventually leads to microshear and adhesion wear [42]. The size of wear debris of the ESD, MAO, and ESD + MAO coatings was found to be not uniform. The plastic deformation, wear debris, and furrow exhibited that the wear mechanism of the ESD surface is similar to bare Ti6Al4V alloy, as seen in Fig. 9b. The wear traces of the ESD coating are relatively shallow compared to bare Ti6Al4V alloy. This implies that the ESD coating provides significant wear resistance to bare Ti6Al4V alloy. The MAO and ESD + MAO coatings mainly consist of oxide-based phases. Thus, the friction action of the counterface eliminated the asperities and smoothened the contact surfaces, as shown in Figs. 9c,d. As a result, any evidence of deformation and scratching has been identified. However, the ESD + MAO coating was worn more than the MAO coating, as seen in Figs. 8, 9c,d. It could be concluded that the lower wear

resistance of the ESD + MAO coating originates from the non-homogeneous, porous, and cracked structure compared to the MAO coating.

4. Conclusions

In this work, intermetallic- and oxide-based duplex coatings were fabricated on Ti6Al4V alloy (ASTM B205-90 Grade 5) by combined ESD and MAO processes. The MAO and ESD + MAO duplex coatings contained oxide-based rutile-TiO_2 and γ-Al_2O_3 phases, while the intermetallic-based Al_3Ti, Al_2Ti, and $AlTi_3$ phases were observed in the ESD coating. The mechanical properties of the coatings were significantly improved compared to bare Ti6Al4V alloy. Through the cross-sectional area, the average Vickers hardness values of bare Ti6Al4V, ESD, and MAO coatings were approximately evaluated as 337.4, 439.4, and 809.1 MPa, respectively. The tribological properties of the coatings were significantly improved compared to bare Ti6Al4V alloy. The average friction coefficient, which was 0.401 in the bare Ti6Al4V sample, decreased to 0.377 in the MAO coatings. The order of the coatings in terms of wear resistance from the highest to the lowest was MAO, ESD, ESD + MAO, and uncoated Ti6Al4V alloy.

Acknowledgements

References

[1] A. K. García-Rueda, D. Guzmán-Castillo, L. García-González, L. Zamora-Peredo, J. Hernández-Torres, Surface modification of a Ti6Al4V alloy by thermal oxidation to improve its tribological properties, Mater. Lett. 317 (2022) 132082.
https://doi.org/10.1016/j.matlet.2022.132082

[2] X. W. Chen, M. L. Li, D. F. Zhang, L. P. Cai, P. Ren, J. Hu, D. D. Liao, Corrosion resistance of MoS_2-modified titanium alloy micro-arc oxidation coating, Surf. Coat. Technol. 433 (2022) 128127.
https://doi.org/10.1016/j.surfcoat.2022.128127

[3] R. Z. Xie, N. M. Lin, P. Zhou, J. J. Zou, P. J. Han, Z. H. Wang, B. Tang, Surface damage mitigation of TC4 alloy via micro-arc oxidation for oil and gas exploitation application: Characterizations of microstructure and evaluations on surface performance, Appl. Surf. Sci. 436 (2018) 467–476.
https://doi.org/10.1016/j.apsusc.2017.12.047

[4] J. T. Philip, D. Kumar, J. Mathew, B. Kuriachen, Tribological investigations of wear resistant layers

developed through EDA and WEDA techniques on Ti6Al4V surfaces: Part II – High temperature, Wear 466 (2021) 203409.
https://doi.org/10.1016/j.wear.2020.203540

[5] Y. C. Bao, W. L. Wang, W. F. Cui, G. W. Qin, Corrosion resistance and antibacterial activity of Ti-N-O coatings deposited on dental titanium alloy, Surf. Coat. Technol. 419 (2021) 127296.
https://doi.org/10.1016/j.surfcoat.2021.127296

[6] Y. S. Cho, L. K. Liao, C. H. Hsu, Y. H. Hsu, W. Y. Wu, S. C. Liao, K. H. Chen, P. W. Lui, S. Zhang, S. Y. Lien, Effect of substrate bias on biocompatibility of amorphous carbon coatings deposited on Ti6Al4V by PECVD, Surf. Coat. Technol. 357 (2019) 212–217.
https://doi.org/10.1016/j.surfcoat.2018.09.070

[7] Z. Q. Liu, X. L. Liu, S. Ramakrishna, Surface engineering of biomaterials in orthopedic and dental implants: Strategies to improve osteointegration, bacteriostatic and bactericidal activities, Biotechnol. J. 16 (2021) 1–23. https://doi.org/10.1002/biot.202000116

[8] A. Anand, M. Das, B. Kundu, V. K. Balla, S. Bodhak, S. Gangadharan, Tribocorrosion characteristics of Ti6Al4V-TiB-TiN in-situ composite coatings prepared using plasma spraying, J. Comp. Mater. 55 (2021) 1935–1946.
https://doi.org/10.1177/0021998320981129

[9] T. K. Cao, S. T. Lei, M. Zhang, The friction and wear behavior of Cu/Cu-MoS_2 self-lubricating coating prepared by electrospark deposition, Surf. Coat. Technol. 270 (2015) 24–32.
https://doi.org/10.1016/j.surfcoat.2015.03.023

[10] W. F. Wang, C. Han, Microstructure and wear resistance of Ti6Al4V coating fabricated by electro-spark deposition, Metals 9 (2019) 23.
https://doi.org/10.3390/met9010023

[11] J. M. Tang, Mechanical and tribological properties of the TiC-TiB_2 composite coating deposited on 40Cr-steel by electro spark deposition, Appl. Surf. Sci. 365 (2016) 202–208.
https://doi.org/10.1016/j.apsusc.2015.12.198

[12] X. Wei, Z. G. Chen, J. Zhong, L. Wang, Z. W. Hou, Y. Zhang, F. L. Tan, Facile preparation of nanocrystalline Fe_2B coating by direct electro-spark deposition of coarse-grained Fe_2B electrode material, J. Alloy. Comp. 717 (2017) 31–40.
https://doi.org/10.1016/j.jallcom.2017.05.081

[13] P. A. Pesode, S. B. Barve, Recent advances on the antibacterial coating on titanium implant by micro-Arc oxidation process, Materials Today: Proceedings 47 (2021) 5652–5662.
https://doi.org/10.1016/j.matpr.2021.03.702

[14] K. Ju, X. Chen, Z. Zhao, Fabrication of $Ti/TiO_2(Ca)$/hydroxyapatite bioceramic material by micro-arc oxidation and electrochemical deposition, Ceram. Int. 48 (2022) 19937–19943.
https://doi.org/10.1016/j.ceramint.2022.03.268

[15] W. Yao, W. Liang, G. Huang, B. Jiang, A. Atrens, F. Pan, Superhydrophobic coatings for corrosion protection of magnesium alloys, J. Mater. Sci. Technol. 52 (2020) 100–118.
https://doi.org/10.1016/j.jmst.2020.02.055

[16] M. Echeverry-Rendon, V. Duque, D. Quintero, M. C. Harmsen, F. Echeverria, Novel coatings obtained by plasma electrolytic oxidation to improve the corrosion resistance of magnesium-based biodegradable

implants, Surf. Coat. Technol. 354 (2018) 28–37.
https://doi.org/10.1016/j.surfcoat.2018.09.007

[17] W. Yao, L. Wu, J. Wang, B. Jiang, D. Zhang, M. Serdechnova, T. Shulha, C. Blawert, M. L. Zheludkevich, F. Pan, Micro-arc oxidation of magnesium alloys: A review, J. Mater. Sci. Technol. 118 (2022) 158–180. https://doi.org/10.1016/j.jmst.2021.11.053

[18] S. Durdu, S. L. Aktug, K. Korkmaz, Characterization and mechanical properties of the duplex coatings produced on steel by electro-spark deposition and micro-arc oxidation, Surf. Coat. Technol. 236 (2013) 303–308. https://doi.org/10.1016/j.surfcoat.2013.10.004

[19] S. Durdu, K. Korkmaz, S. L. Aktug, A. Cakir, Characterization and bioactivity of hydroxyapatite-based coatings formed on steel by electro-spark deposition and micro-arc oxidation, Surf. Coat. Technol. 326 (2017) 111–120. https://doi.org/10.1016/j.surfcoat.2017.07.039

[20] A. Cakir, K. Korkmaz, E. S. Kayali, Study on the Al_2O_3/Fe-Al intermetallic duplex coating prepared with a combined technique of electro-spark deposition and micro-arc oxidation on steel, Kovove Mater. 55 (2017) 81–87. https://doi.org/10.4149/km_2017_2_81

[21] A. V. Ribalko, K. Korkmaz, O. Sahin, Intensification of the anodic erosion in electrospark alloying by the employment of pulse group, Surf. Coat. Technol. 202 (2008) 3591–3599. https://doi.org/10.1016/j.surfcoat.2007.12.037

[22] F. P. J. Machado, A. N. Luiggi, Study of electronic properties of Al_3Ti, AlTi and $AlTi_3$ intermetallic compounds using DFT-FPLAPW, J. Computation. Method. Sci. Eng. 14 (2014) 53–71. https://doi.org/10.3233/jcm-130484

[23] A. L. Yerokhin, X. Nie, A. Leyland, A. Matthews, S. J. Dowey, Plasma electrolysis for surface engineering, Surf. Coat. Technol. 122 (1999) 73–93. https://doi.org/10.1016/s0257-8972(99)00441-7

[24] X. Hong, Y. F. Tan, X. L. Wang, T. Xu, L. Gao, Microstructure and wear resistant performance of TiN/Zr-base amorphous-nanocrystalline composite coatings on titanium alloy by electrospark deposition, Surf. Coat. Technol. 305 (2016) 67–75. https://doi.org/10.1016/j.surfcoat.2016.07.077

[25] X. X. Zhang, L. Yang, X. Q. Lu, Y. Lv, D. Jiang, Y. Yu, Z. Peng, Z. H. Dong, Characterization and property of dual-functional Zn-incorporated TiO_2 micro-arc oxidation coatings: The influence of current density, J. Alloy. Comp. 810 (2019) 151893. https://doi.org/10.1016/j.jallcom.2019.151893

[26] R. Y. Wang, T. Zhou, J. Liu, X. W. Zhang, F. Long, L. Liu, Bilayer microstructure of antibacterial TiO_2 coating on Ti6Al4V fabricated via micro-arc oxidation in W-containing electrolytes, Surf. Coat. Technol. 413 (2021) 127094. https://doi.org/10.1016/j.surfcoat.2021.127094

[27] W.-F. Wang, M.-C. Wang, F.-J. Sun, Y.-G. Zheng, J.-M. Jiao, Microstructure and cavitation erosion characteristics of Al-Si alloy coating prepared by electrospark deposition, Surf. Coat. Technol. 202 (2008) 5116-5121. https://doi.org/10.1016/j.surfcoat.2008.05.013

[28] M. Roostaei, H. Aghajani, M. Abbasi, B. Abasht, Formation of Al_2O_3/MoS_2 nanocomposite coatings by the use of electro spark deposition and oxidation, Ceram. Int. 47 (2021) 11644–11653. https://doi.org/10.1016/j.ceramint.2020.12.296

[29] X. J. Li, M. Zhang, S. Wen, X. Mao, W. G. Huo, Y. Y. Guo, Y. X. Wang, Microstructure and wear resistance of micro-arc oxidation ceramic coatings prepared on 2A50 aluminum alloys, Surf. Coat. Technol. 394 (2020) 125853. https://doi.org/10.1016/j.surfcoat.2020.125853

[30] G. Sundararajan, L. Rama Krishna, Mechanisms underlying the formation of thick alumina coatings through the MAO coating technology, Surf. Coat. Technol. 167 (2003) 269–277. https://doi.org/10.1016/S0257-8972(02)00918-0

[31] S. L. Aktug, S. Durdu, S. Aktas, E. Yalcin, M. Usta, Characterization and investigation of in vitro properties of antibacterial copper deposited on bioactive ZrO_2 coatings on zirconium, Thin Solid Films 681 (2019) 69–77. https://doi.org/10.1016/j.tsf.2019.04.042

[32] C. Wang, J. Hong, M. Cui, H. Huang, L. Zhang, J. Yan, The effects of simultaneous laser nitriding and texturing on surface hardness and tribological properties of Ti6Al4V, Surf. Coat. Technol. 437 (2022) 1–11. https://doi.org/10.1016/j.surfcoat.2022.128358

[33] G. Fowler, I. R. Pashby, P. H. Shipway, The effect of particle hardness and shape when abrasive water jet milling titanium alloy Ti6Al4V, Wear 266 (2009) 613–620. https://doi.org/10.1016/j.wear.2008.06.013

[34] D. Liu, W. Gao, Z. Li, H. Zhang, Z. Hu, Electrospark deposition of Fe-based amorphous alloy coatings, Mater. Lett. 61 (2007) 165–167. https://doi.org/10.1016/j.matlet.2006.04.042

[35] D. T. Asquith, A. L. Yerokhin, J. R. Yates, A. Matthews, Effect of combined shot-peening and PEO treatment on fatigue life of 2024 Al alloy, Thin Solid Films 515 (2006) 1187–1191. https://doi.org/10.1016/j.tsf.2006.07.123

[36] J. A. Curran, T. W. Clyne, The thermal conductivity of plasma electrolytic oxide coatings on aluminium and magnesium, Surf. Coat. Technol. 199 (2005) 177–183. https://doi.org/10.1016/j.surfcoat.2004.11.045

[37] E. Matykina, R. Arrabal, P. Skeldon, G. E. Thompson, Investigation of the growth processes of coatings formed by AC plasma electrolytic oxidation of aluminium, Electrochim. Acta 54 (2009) 6767–6778. https://doi.org/10.1016/j.electacta.2009.06.088

[38] S. Durdu, O. F. Deniz, I. Kutbay, M. Usta, Characterization and formation of hydroxyapatite on Ti6Al4V coated by plasma electrolytic oxidation, J. Alloys Comp. 551 (2013) 422–429. https://doi.org/10.1016/j.jallcom.2012.11.024

[39] Y.-J. Oh, J.-I. Mun, J.-H. Kim, Effects of alloying elements on microstructure and protective properties of Al_2O_3 coatings formed on aluminum alloy substrates by plasma electrolysis, Surf. Coat. Technol. 204 (2009) 141–148. https://doi.org/10.1016/j.surfcoat.2009.07.002

[40] Y. Han, J. F. Sun, X. Huang, Formation mechanism of HA-based coatings by micro-arc oxidation, Electrochem. Comm. 10 (2008) 510–513. https://doi.org/10.1016/j.elecom.2008.01.026

[41] J. Kováčik, P. Baksa, Š. Emmer, Electro spark deposition of TiB_2 layers on Ti6Al4V alloy, Acta Metallurgica Slovaca 22 (2016) 52–59. https://doi.org/10.12776/ams.v22i1.628

[42] M. Khorasanian, A. Dehghan, M. H. Shariat, M. E. Bahrololoom, S. Javadpour, Microstructure and wear

resistance of oxide coatings on Ti-6Al-4V produced by plasma electrolytic oxidation in an inexpensive electrolyte, Surf. Coat. Technol. 206 (2011) 1495–1502. https://doi.org/10.1016/j.surfcoat.2011.09.038